LETTER

Heterostructured Gel Polymer Electrolyte Enabling Long-Cycle Quasi-Solid-State Lithium Metal Batteries

Shaolun Cui, Xuewen Wu, Yang Yang, Minfei Fei, Sheng Liu, Guoran Li,* and Xue-Ping Gao

Read Online

ACCESS | Metrics & More | Article Recommendations | Supporting Information

ABSTRACT: For rechargeable lithium−metal batteries (RLBs), gel polymer electrolytes (GPEs) are a very competitive and pragmatic option because the special composite structure could restrain the uncontrolled lithium dendrite in a liquid electrolyte and avoid the poor interface contact for a solid-state electrolyte. However, the difficulty lies in finding a delicate balance between ion transport and interface stability. Herein, a heterostructured GPE, in which a metal−organic framework layer and an ultrathin Al_2O_3 deposition are coated on the same side of a polymer matrix, is fabricated to homogenize lithium ion transport and stabilize the lithium anode interface. With the heterostructured GPE, the Li^+ transference number is improved to 0.74, and the lithium metal electrode displays an enhanced cycle stability over 1000 h. Moreover, Li-rich Mn-based layered oxides, the high-capacity cathode material, are matched for the first time with a lithium−metal anode to assemble a quasi-solid-state RLB, which delivers an initial discharge capacity of 257.5 mAh g^{-1} with a long-cycle capacity retention of 84.6% after 500 cycles at a rate of 0.2C.
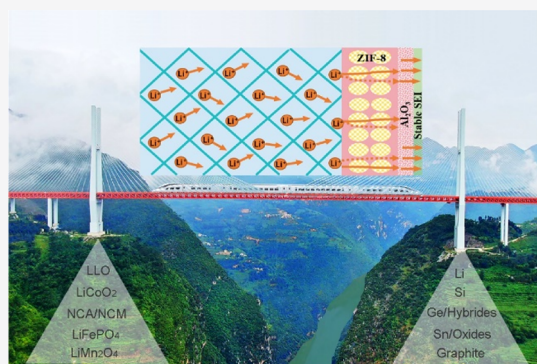
etallic lithium has attracted extensive research attention as a promising anode material for rechargeable lithium−metal batteries (RLBs) with a large theoretical specific capacity of 3860 mAh g^{-1} and low reduction potential (−3.04 V vs standard hydrogen electrode).[1−3] It is expected to build RLBs with high energy and power density to meet the increasing demands of future electronic equipment and electric vehicles. However, the lithium anode tends to trigger parasite reactions with the traditional organic liquid electrolyte due to its excessive reaction activity during the charge/discharge process.[4] Especially, the continuous and nonuniform plating/stripping characteristics of Li during cycling can result in lithium dendrite formations. The uncontrolled lithium dendrites cause not only a reduction of the Coulombic efficiency but also serious safety hazards.[5−8] Therefore, numerous attempts are devoted to the development of new electrolytes such as inorganic solid electrolytes (ISEs), solid polymer electrolytes (SPEs), and gel polymer electrolytes (GPEs) in order to solve the inherent problems of leakage, flammability, and volatilization in conventional liquid electrolytes.[9−13]

GPEs stand out from the choice of solid-state systems due to their high flexibility, light weight, easy manufacturing, and superior interface compatibility in contrast to the rigidity and fragility of ISEs and the nonflowing characteristics of SPEs.[14,15]

Nevertheless, GPEs usually suffer from poor mechanical strength and unsatisfactory ionic conductivity, which cannot completely inhibit the nucleation and growth of lithium dendrites.[16] Generally, the nucleation and growth processes of lithium dendrites are closely related to the transference number of lithium ions and anions. A higher Li^+ transference number can prolong the Sand's time and hinder the free migration of anions, contributing to homogeneous lithium deposition.[17] Besides, the highly active metallic lithium reacts with the electrolyte to form a solid electrolyte interface (SEI) film, and lithium ions can be deposited through the SEI film.[17,18] The interfacial component, structure, and characteristics will also directly affect the rapid transport of lithium ions and play an important role in stabilizing the lithium anode. Thus, optimizing the electrolyte structure with a stable interface compatibility, high Li^+ transference number, and robust mechanical strength is an effective strategy for achieving a uniform lithium deposition and constructing high-safety
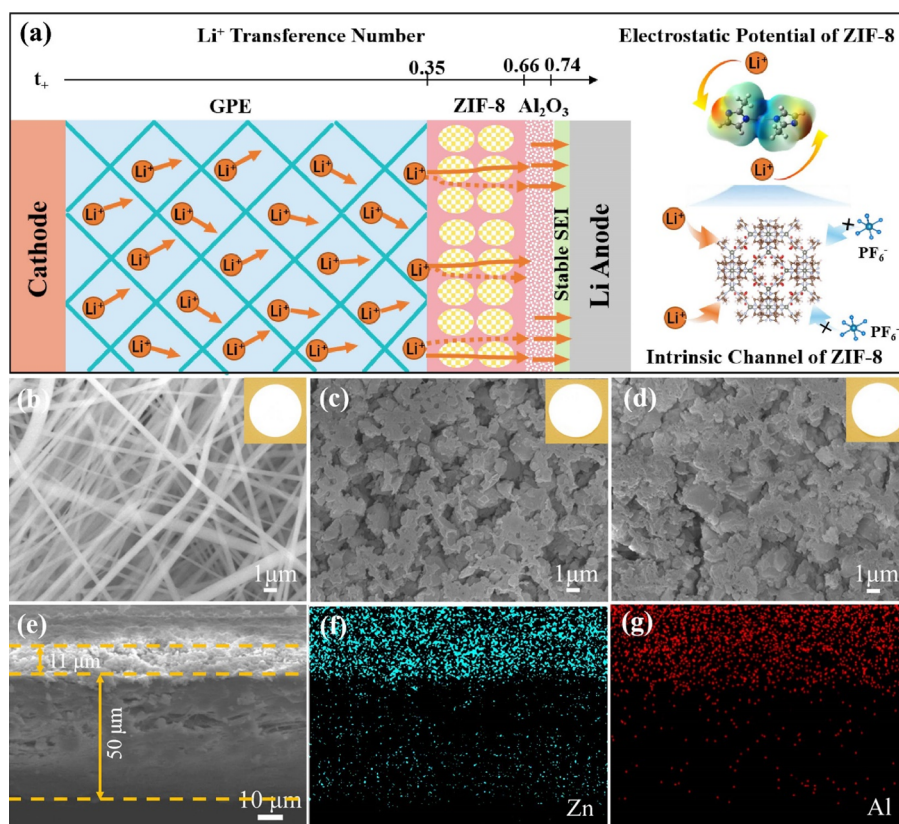
Figure 1. (a) Schematic diagram of the heterostructured GPE, increase of lithium ion transference number with the varying structure, and electrostatic potential distribution and intrinsic channel of ZIF-8. (b−d) SEM images and optical images of as-prepared (b) GPE, (c) GPE-ZIF8, and (d) GPE-ZIF8-Al$_2$O$_3$ films, respectively. (e) Cross-sectional SEM image of the GPE-ZIF8-Al$_2$O$_3$ film. (f, g) Corresponding EDS-mapping results.

RLBs.[19−21] At present, the construction of composite electrolytes based on the synergy between inorganic ceramic fillers and polymer components has become a viable strategy for a comprehensive performance,[22−24] whereas an addition of ceramic fillers to the polymer electrolyte can easily cause aggregation and phase separation in the matrix, especially when nanoparticles exceed a certain size and content, thereby influencing the ionic conductivity and energy density of the battery.[25] Additionally, the latest research shows that ions can only move along the edge of the polymer matrix and the filler because ions would not transfer through the bulk phase of the inorganic filler, which also limits the effect of the composite polymer electrolyte in improving the ion transport.[26−28] In order to better support the advantages of ceramic fillers and polymer electrolytes, multilayered structures should be necessary to build a stable interface with a lower diffusion barrier while regulating the ion transport.

Herein, a new type of heterostructured GPE is shown, in which a metal−organic framework (MOF) layer and atomic layer-deposited Al$_2$O$_3$ are modified on one side of the polymer matrix to tailor the lithium ion transport and interface stability. MOFs are widely applied as lithium hosts and electrolyte fillers to improve ion transport and charge transfer processes due to their large specific surface area, stable skeletons, well-defined pore pathways, and abundant Lewis acid sites, thereby inhibiting the formation of lithium dendrites.[29,30] Moreover, Al$_2$O$_3$ as an electrolyte additive[31] and inert ceramic filler[32] has been proven to improve the physical and chemical properties of electrolytes, while in the heterostructured GPEs, the ZIF-8

and Al$_2$O$_3$ layer will act as a "traffic commander", which regulates a uniform lithium ion flux to contribute the ion transport as well as enables a high mechanical strength to inhibit the growth of lithium dendrites. It is worth pointing out that the imidazole molecule of ZIF-8 particles can bind with Li$^+$ via a nucleophilic effect to prolong the lithium nucleation time and that defined nanosized channels can restrict the free migration of anions. Meanwhile, the inert Al$_2$O$_3$ nanocoating obtained by atomic layer deposition (ALD) can not only enhance the affinity with the lithium anode but also participate in the buildup of the solid-electrolyte interface (SEI) film and lower the diffusion barrier of lithium ions. On the basis of the synergistic effect, the Li$^+$ transference number increases from 0.35 to 0.74, and the Li symmetric cell with the heterostructured GPEs exhibits superior plating/stripping reversibility over 1000 h. Furthermore, for the first time, solid-state RLBs coupled with Li-rich Mn-based cathode materials with a wide voltage range of 2.0−4.8 V are reported, and a capacity retention of 84.6% is realized after 500 cycles at the rate of 0.2C, showing an outstanding electrochemical performance among the previous GPEs-based solid-state RLBs.

The schematic diagrams of the fabrication and design concept of the heterostructured gel polymer electrolytes, marked as GPE-ZIF8-Al$_2$O$_3$, are shown in Figure S1 (Supporting Information) and Figure 1a, respectively. The GPE matrix composed of poly(vinylidene fluoride-*co*-hexa-fluoropropylene) (PVDF-HFP), cellulose acetate (CA), and succinonitrile (SN) is obtained by an electrospinning method. Among them, PVDF-HFP owns a relatively higher ionic
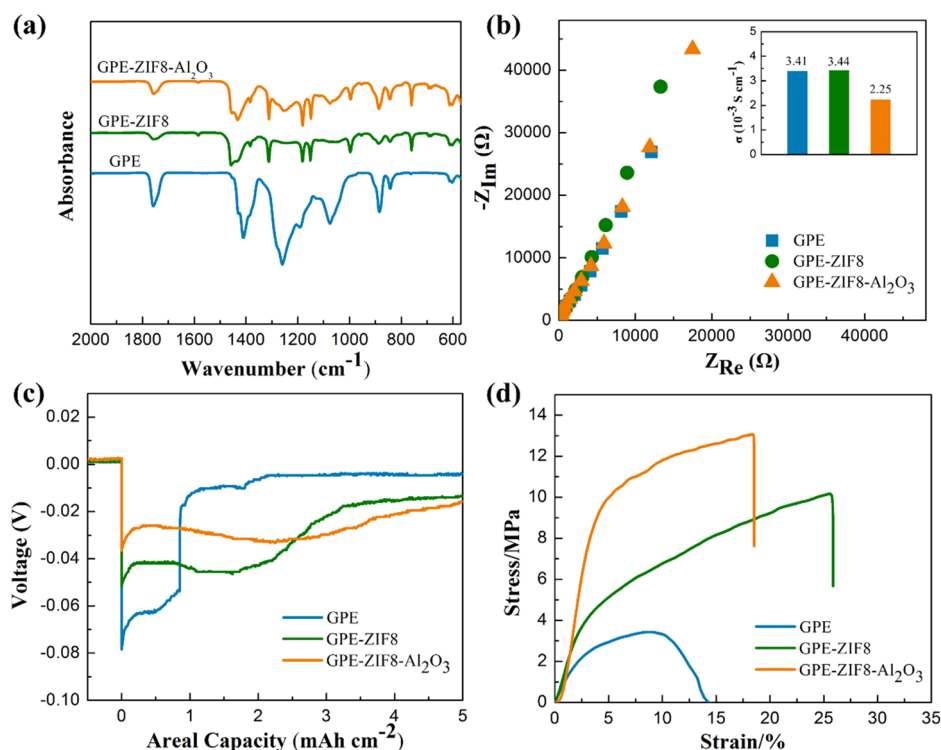
Figure 2. (a) Diffuse reflectance infrared spectra of GPE, GPE-ZIF8, and GPE-ZIF8-Al$_2$O$_3$ films. (b) AC impedance plots and (inset) corresponding ionic conductivity histograms. (c) Nucleation overpotentials of lithium. (d) Representative stress−strain curves for GPE, GPE-ZIF8, and GPE-ZIF8-Al$_2$O$_3$ films.

conductivity and lower crystallinity, while CA can enhance the mechanical strength of the polymer matrix.[33] Through the swelling effect of the electrolyte solvents, a liquid absorption rate of up to 300% can be achieved in the polymer network system, and our previous study verifies an intimate contact between the GPE matrix and cathode materials.[34] Then the solution containing ZIF-8 nanoparticles after an ultrasonic dispersion is uniformly casted on one side of the GPE substrate, and the gel polymer electrolyte modified with ZIF-8 (GPE-ZIF8) is prepared after the solvent evaporates. It is reported that ZIF-8 nanoparticles characterized by the thermal stability, robust skeleton, and permanent porosity own a large specific surface area (up to 1499 m^2 g^{-1}) and a well-defined pore structure (large cavities of 11.6 Å and small apertures of 3.4 Å).[35,36] Moreover, the final GPE-ZIF8-Al$_2$O$_3$ film is gained by adding an ultrathin Al$_2$O$_3$ layer on the same side as ZIF-8 by atomic layer deposition. The regulation of lithium ion transport in the heterostructured electrolyte can be demonstrated on the basis of the Li$^+$ transference numbers (Figure S2 and Table S1, Supporting Information). Limited by the strong solvation effect, the lithium ions in the GPE film are transported through the gap channels between the polymer fibers and exhibit a low Li$^+$ transference number of 0.35.[37] According to the electrostatic potential distribution of ZIF-8 (Figure 1a), the large electron cloud density of the N atom on the imidazole molecule away from the Zn^{2+} indicates strong electronegativity and nucleophilicity, which can coordinate with lithium ions to facilitate the rapid transport through internal channels. Benefiting from the intrinsic confined nanochannels of MOFs, the migration of anions (PF$_6^-$) with a relatively larger radius is restricted to a certain extent.[38] Under the synergy, the main migration path of lithium ions in the ZIF-8 layer will depend on the intrinsic nanochannels, and

the Li$^+$ transference number in the GPE-ZIF8 film can be as high as 0.66. The deposited Al$_2$O$_3$ layer can increase the Li$^+$ transference number to 0.74 and inhibit the excessive reactivity of the lithium anode through the interface layer construction, which will be explored in the following discussion. Figure 1b−d shows the scanning electron microscope (SEM) images and optical images of as-prepared GPE, GPE-ZIF8, and GPE-ZIF8-Al$_2$O$_3$ films, respectively. It can be observed in Figure 1b that the GPE matrix is composed of fibers with a diameter of 0.5−1 μm, in which the relatively high porosity can support ion diffusion. And the Energy dispersive spectroscopy (EDS)-mapping results (Figure S3, Supporting Information) demonstrate that C, O, and F elements are uniformly distributed in the fibers. After casting ZIF-8 nanoparticles, it is clear to see that one side of the GPE-ZIF8 film is fully covered by ZIF-8 particles with an average grain size of 0.5−1 μm, as shown in Figure 1c. Furthermore, no significant changes are observed on the surface of the ZIF-8 modified layer despite the deposition of Al$_2$O$_3$ in Figure 1d. It is demonstrated that a nanoscale ultrathin Al$_2$O$_3$ layer is formed on the surface of the substrate through the ALD technology. The comparative analysis of the optical images of different electrolyte films shows that neither the slurry coating nor the Al$_2$O$_3$ deposition will make significant differences in the apparent colors. From the cross-sectional image of the GPE-ZIF8-Al$_2$O$_3$ film in Figure 1e, the GPE substrate (a thickness of 50 μm) maintains compact contact with the coating layer (a thickness of 11 μm). The corresponding EDS-mapping results of the Zn element attributed to ZIF-8 nanoparticles and the Al element derived from Al$_2$O$_3$ deposition, as displayed in Figure 1f,g, further demonstrate that the ZIF-8 nanoparticles are uniformly covered on the polymer matrix and that Al$_2$O$_3$ is deposited on the surface of the ZIF-8 layer.
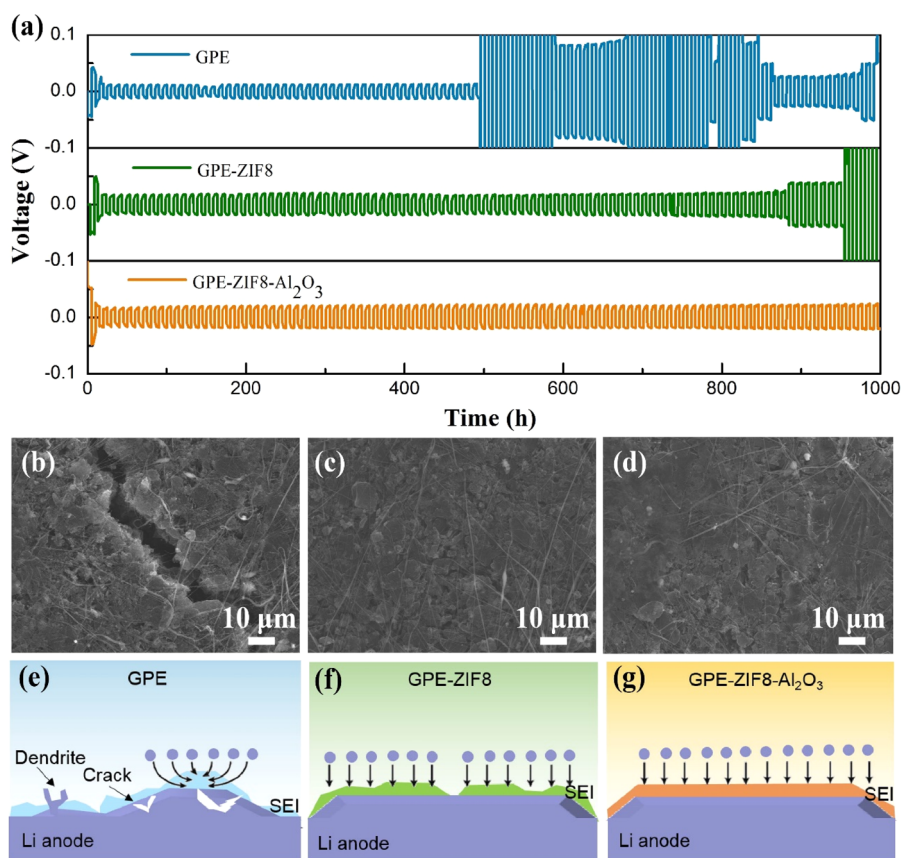
Figure 3. Electrochemical cycling tests, surface morphologies of lithium deposition, and schematic diagrams based on the Li/Li symmetric cells with GPE, GPE-ZIF8, and GPE-ZIF8-Al$_2$O$_3$ films. (a) Voltage profiles of Li/GPE/Li, Li/GPE-ZIF8/Li, and Li/GPE-ZIF8-Al$_2$O$_3$/Li symmetric cells at 0.2 mA cm^{-2} for 1 mAh cm^{-2}. SEM images of the surface morphology of a Li electrode after plating/stripping for 1000 h at 0.2 mA cm^{-2} for 1 mAh cm^{-2} in the (b) GPE, (c) GPE-ZIF8, and (d) GPE-ZIF8-Al$_2$O$_3$ films. Schematic diagrams of the microscopic mechanism during the lithium deposition process for (e) GPE, (f) GPE-ZIF8, and (g) GPE-ZIF8-Al$_2$O$_3$ films.

Author: Please verify that the changes made to improve the English still retain your original meaning. The diffuse reflectance infrared spectra in the range of 2000−600 cm^{-1} are conducted to further confirm the structural composition of the heterostructured GPE film (Figure 2a). In the infrared spectrum of the GPE film, the bond in the 1410 cm^{-1} region corresponds to the bending vibration of the −CH$_2$ group in PVDF-HFP, while the bonds at 1750 and 1260 cm^{-1} correspond to the vibrational absorption peak of C=O and the characteristic absorption of C−O, respectively, indicating the ester group in cellulose acetate.[39,40] After casting the ZIF-8 nanoparticles, the weak peak that appeared at 1580 cm^{-1} is attributed to the stretching C=N vibration of imidazole, whereas the intense and convoluted peaks at 1500−1000 cm^{-1} can be assigned as the ring stretching area.[41,42] For the GPE-ZIF8 film, the peak intensity at 1750 cm^{-1} significantly weakens due to the coating of ZIF-8 nanoparticles on the surface of the GPE film. It is related not only to the fact that ZIF-8 nanoparticles coated on the outer layer do not contain C=O functional groups but also to the fact that this composite electrolyte structure will reduce the crystallinity of the polymer matrix, thereby weakening the corresponding peak intensity. The infrared spectrum of the GPE-ZIF8-Al$_2$O$_3$ film is almost the same as that of the GPE-ZIF8 film, but the signal associated with C=N for ZIF-8 decreases because of the ultrathin Al$_2$O$_3$ layer on the surface. Furthermore, the surface composition of the GPE-ZIF8-Al$_2$O$_3$ film is confirmed by X-

ray photoelectron spectroscopy (XPS), as shown in Figure S4 (Supporting Information). Besides the signals of Zn 2p at 1045.50 and 1022.35 eV, the peak at 74.40 eV attributed to Al−O bonds clearly reveals that the Al$_2$O$_3$ layer is successfully deposited on the surface of the GPE-ZIF8-Al$_2$O$_3$ film.[43,44]

For the heterostructure, an important concern is how the coating layers influence ionic conductivity, which plays a pivotal role in the electrode reaction kinetics.[10] The ionic conductivity of the different films is calculated through the bulk resistance from the impedance spectra shown in Figure 2b (the detailed data are listed in Table S2, Supporting Information). For the pristine GPE film, the ionic conductivity is 3.41 × 10^{-3} S cm^{-1}, and the value is negligibly improved to 3.44 × 10^{-3} S cm^{-1} for the GPE-ZIF8 film. This can be attributed to the strong nucleophilicity of the metal−organic framework mentioned above. When Al$_2$O$_3$ is further coated, the GPE-ZIF8-Al$_2$O$_3$ film has a slightly declined ionic conductivity of 2.25 × 10^{-3} S cm^{-1}, since Al$_2$O$_3$ is not an active ion conductor. However, for a lithium ion battery, the effective conductivity should be equal to the measured total conductivity times the Li$^+$ transference number.[45] Therefore, the effective conductivity for GPE, GPE-ZIF8, and GPE-ZIF8-Al$_2$O$_3$ films is 1.19 × 10^{-3}, 2.27 × 10^{-3}, and 1.67 × 10^{-3} S cm^{-1}, respectively. Compared with GPE, GPE-ZIF8-Al$_2$O$_3$ actually provides an improved effective conductivity, and even compared with GPE-ZIF8, it keeps the comparable value. The more important role of the Al$_2$O$_3$ thin layer in stabilizing
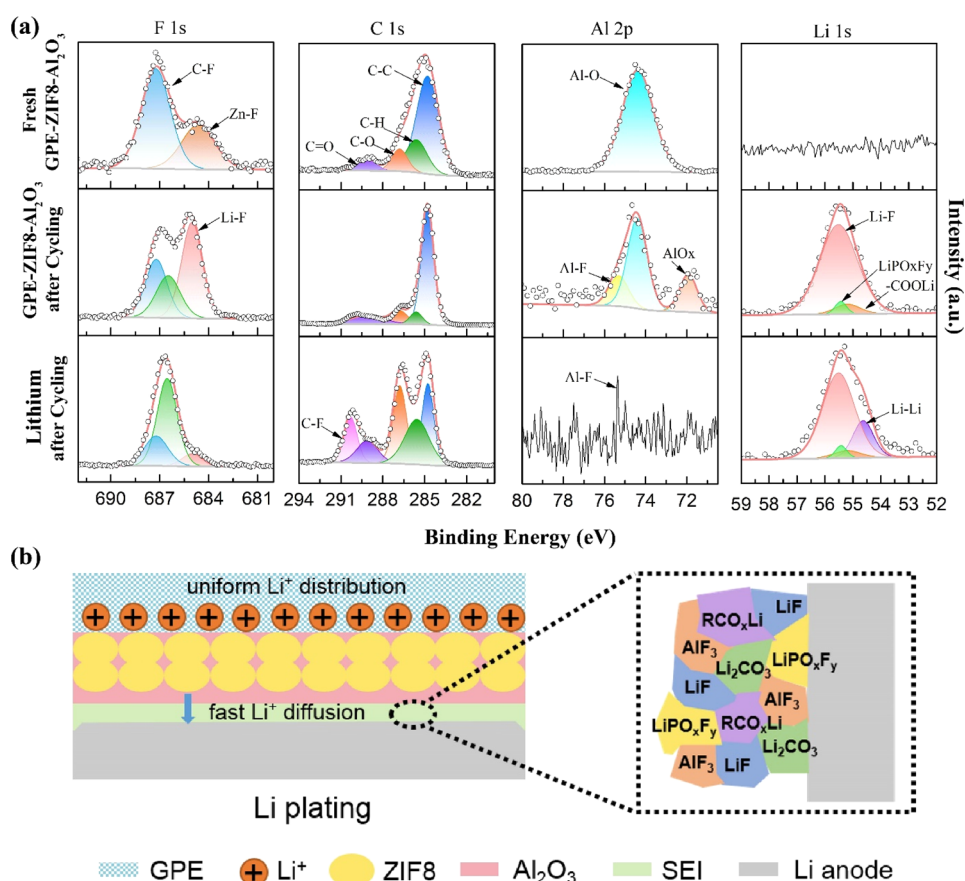
Figure 4. (a) XPS spectra of F 1s, C 1s, Al 2p, and Li 1s for the fresh GPE-ZIF8-Al$_2$O$_3$ film, cycled GPE-ZIF8-Al$_2$O$_3$ film, and cycled lithium anode in the symmetric cells. (b) Schematic illustrations of SEI components formed on the interface between GPE-ZIF8-Al$_2$O$_3$ film and Li anode.

the lithium anode interface will be discussed below. The cyclic voltammetry (CV) tests with a wide voltage range from −0.5 to 5.0 V are performed to investigate the electrochemical stability of different electrolytes (see Figure S5). The reduction peak at −0.5 V represents the deposition of lithium ions on stainless steel, and the oxidation signal at 0.3 V represents the dissolution of lithium. It is found that no redox peak appears in the polymer electrolytes, indicating a wide and stable electrochemical window before and after a modification.

Besides the effective conductivity, the dissolution and deposition kinetics of lithium at the interface is also influenced by the heterostructure. The nucleation overpotential of lithium, which is defined as the difference between the lowest voltage and the discharge plateau in the transient nucleation stage of the initial lithium deposition, can reflect the nucleation barrier of lithium deposition.[46,47] As shown in Figure 2c, the nucleation overpotential in the GPE-ZIF8-Al$_2$O$_3$ case exhibits the lowest value of 20.4 mV, while the value for GPE-ZIF8 and GPE is 36.9 and 73.7 mV, respectively. The results show that the ZIF-8 nanoparticles and Al$_2$O$_3$ thin layer are not only beneficial for a transference of lithium ions but also make lithium deposition relatively easy. This can be attributed to the homogenization effect of lithium ion transport and the desolvation effect of the two coating layers.[48] In addition, the mechanical strength is also important for the composite films to inhibit the growth of lithium dendrites. The stress–strain test results shown in Figure 2d verify that the maximum tensile strength of the GPE film is only 3.43 MPa, and the

parameter of the GPE-ZIF8 and GPE-ZIF8-Al$_2$O$_3$ films is obviously increased to 10.17 and 13.08 MPa, respectively. From the slope of the stress–strain curve, it can be concluded that GPE-ZIF8-Al$_2$O$_3$ possesses a higher tensile modulus, meaning a more excellent resistance to an elastic deformation.

The influence of the electrolytes on the long-term cycling stability of lithium electrodes is investigated by the Li/GPE/Li, Li/GPE-ZIF8/Li, and Li/GPE-ZIF8-Al$_2$O$_3$/Li symmetric cells (Figure 3a). All the symmetric cells are charged and discharged at a current density of 0.2 mA cm^{-2} with an areal capacity of 1 mAh cm^{-2}. For Li/GPE/Li, despite a relatively low over-potential in the initial few cycles, the polarization voltage sharply increases after 490 h, meaning the occurrence of a partial short circuit at the galvanostatic measurement. Interestingly, after the cycle is continued for hundreds of hours, the large polarization voltage has a sudden drop irregularly. It can be deduced that lithium dendrite forms and penetrates the GPE film to cause the partial short circuit at 490 h, and the lithium dendrite could break with the subsequent cycling. Li/GPE-ZIF8/Li maintains a stable cycle performance over 880 h, and the value of polarization voltage tends to 22 mV. However, in the next few cycles, the polarization voltage increases suddenly to 38 mV, and then an obvious short circuit occurs. The result shows that the introduction of ZIF-8 indeed plays a role in inhibiting the growth of lithium dendrites to a certain extent. Most importantly, as a sharp contrast, Li/GPE-ZIF8-Al$_2$O$_3$/Li achieves stable cycling over 1000 h with a continuously small polarization voltage of ∼20 mV. Combined

with the analysis in the previous paragraph, it is believed that a robust interface between GPE-ZIF8-Al_2O_3 and a lithium anode is generated with the participation of Al_2O_3, thereby effectively regulating the nucleation and growth process of lithium deposition and inhibiting the formation of lithium dendrites. Subsequently, a larger current density of 1 mA cm^{-2} is applied to test the superiority of cycle stability in GPE-ZIF8-Al_2O_3 film (Figure S6, Supporting Information), in which the polarization voltage keeps a steady increase to no more than 100 mV after 300 h and shows an excellent reversibility of lithium plating-stripping. The Li/Cu cell of GPE-ZIF8-Al_2O_3 also verifies a high and stable Coulombic efficiency over 50 cycles with the capacity of 1 mAh cm^{-2} at the current density of 0.5 mA cm^{-2}, demonstrating the improved reversibility for Li plating/stripping.

Correspondingly, the surface SEM images of the lithium electrodes after cycling for 1000 h are shown in Figure 3b−d. Before cycling (Figure S8, Supporting Information), the fresh lithium electrode presents a smooth surface with a flat microscopic morphology. In the case of Li/GPE/Li, the originally smooth lithium surface becomes rough and porous; in particular, some cracks up to hundreds of microns can be clearly observed (Figure 3b). This kind of crack usually arises from the buildup and release in local stress caused by an uneven lithium depositon.[4,49] Coupled with the weak mechanical strength of the GPE film, the newly deposited fragile active lithium will produce serious cracks and aggravate this phenomenon. In the cases of Li/GPE-ZIF8/Li and Li/GPE-ZIF8-Al_2O_3/Li, the surface morphologies of the lithium electrode facing the ZIF-8 and Al_2O_3 layers are flat and compact (Figure 3c,d), showing that the two can effectively inhibit the generation of an internal stress and achieve a uniform lithium deposition. To better understand the influence of the heterostructure, the schematic diagrams for lithium deposition are shown in Figure 3e−g. For GPE, the uneven ion transport and the relatively high energy barrier of lithium deposition always tend to deposit lithium on some certain places like edges, steps, and protrusions of lithium, which usually have a relatively high electron density. Running repeatedly, lithium dendrites and cracks form inevitably during a long cycling process. The strong nucleophilicity and open channel of the ZIF-8 framework in the GPE-ZIF8 film can effectively regulate the distribution of lithium ion flux and reduce the energy barrier of lithium deposition. Further, the deposited Al_2O_3 for the GPE-ZIF8-Al_2O_3 film can significantly promote the interface stability for lithium electrodes and support a long-term stable cycling. The improvement of interface stability is mainly attributed to the participation of Al_2O_3 in the formation of the SEI, which will be detailedly discussed below.

The XPS spectra of the GPE-ZIF8-Al_2O_3 film and Li electrode before and after cycling in the symmetric cells are obtained to reveal the effect of Al_2O_3 on the interface (Figure 4a). For the fresh GPE-ZIF8-Al_2O_3 film, the main signal of F 1s located at 687.2 eV is from C−F bonds of PVDF-HFP, and the shoulder peak that appeared at 684.6 eV can be well-attributed to Zn−F bonds, suggesting there is a strong interfacial interaction between the ZIF-8 layer and polymer matrix.[50] The signals of C 1s located at 284.8, 285.6, 286.8, and 289.1 eV are assigned to C−C, C−H, C−O, and C=O bonds of ZIF-8 and CA, respectively.[51] Moreover, the single peak of Al 2p of Al_2O_3 appears at 74.4 eV.[52] On the one side, after the system is cycled for 1000 h, the main signal of F 1s of

GPE-ZIF8-Al_2O_3 appears at 685.0 eV, and a single peak for Li 1s, meanwhile, rises at 55.6 eV, clearly declaring the formation of LiF.[53] On the other side, the XPS signal of LiF can also be observed for the cycled lithium electrode. More importantly, for the GPE-ZIF8-Al_2O_3 after cycling, the signals of F 1s at 686.5 eV and Al 2p at 75.3 eV confirm the generation of AlF_3 at the interface. As pointed out in the previous studies, the fluorides, especially LiF and AlF_3, are beneficial for lowering the diffusion energy barrier to ensure a fast diffusion rate and strengthen the mechanical properties of the SEI film during cycling.[54,55] A noteworthy result is the signal of AlO_x in GPE-ZIF8-Al_2O_3 after cycling. Apparently, this is caused by lithium partially reducing Al_2O_3 at the interface of both.[1,56] The F 1s spectrum of the lithium electrode and the Li 1s spectrum of GPE-ZIF8-Al_2O_3 after being cycled are actually very complicated because these spectra could contain the signals of organic salt besides LiF and AlF_3. However, from the C 1s spectrum of the lithium electrode, it can be found that C−F, C=O, C−O, C−H, and C−C bonds appear in the surface of lithium after cycling. This means that the SEI film is composed of multiple components including Li_2CO_3 and RCO_xLi, etc.[53] In addition, the Zn 2p spectra of the cycled GPE-ZIF8-Al_2O_3 film reveals that the ZIF-8 modification layer keeps a stable framework without any composition change during the electrochemical process (Figure S9, Supporting Information).

Figure 4b illustrates the formation of the SEI film on the interface of the lithium electrode involving Al_2O_3. Among the imidazole molecules contained in the ZIF-8 skeleton, the N atom at one end contains a lone pair of electrons, which possesses strong nucleophilicity and electronegativity to stabilize Li$^+$, thereby prolonging the nucleation time during a lithium deposition and achieving a uniform distribution. The Al_2O_3 deposited on the outermost layer can effectively enhance the affinity with the lithium electrode and reduce the nucleation overpotential, contributing to inhibit the nucleation and growth process of lithium dendrites. Particularly, the outermost Al_2O_3 will interact with the $LiPF_6$ to convert from inert, nonconductive oxides to highly conductive fluorides during cycling. In this case, a robust ion-conductive LiF-rich and AlF_3-rich SEI layer would be formed at the Li electrode interface, which will greatly promote the charge transfer process to achieve a uniform lithium deposition and long lifespan. The chemical composition of the SEI layer on the interface of lithium roughly given is supposed to be a complicated multicomponent structure. Besides common organic species, the SEI film rich in LiF and AlF_3 can lower the diffusion barrier of lithium ions and enhance the mechanical strength of the SEI layer. This not only contributes to provide an abundant Li$^+$ supplement and a continuous transport path but also suppresses the formation of lithium dendrites.

To further support the above analysis, the changes at the interface, including the distribution of molecular fragments and functional groups, are characterized by time-of-flight secondary ion mass spectrometry (TOF-SIMS).[57] As a highly surface-sensitive technology, TOF-SIMS depth profiles and two-dimensional (2D) surface scan measurements are conducted in the fresh and cycled GPE-ZIF8-Al_2O_3 films to obtain visual images of surface secondary ion fragments. As the sputtering time increases, the major F element that constitutes the fresh GPE-ZIF8-Al_2O_3 film surface exhibits a steady intensity and content throughout the sputtering depth, while other containing elements and groups maintain a relatively uniform
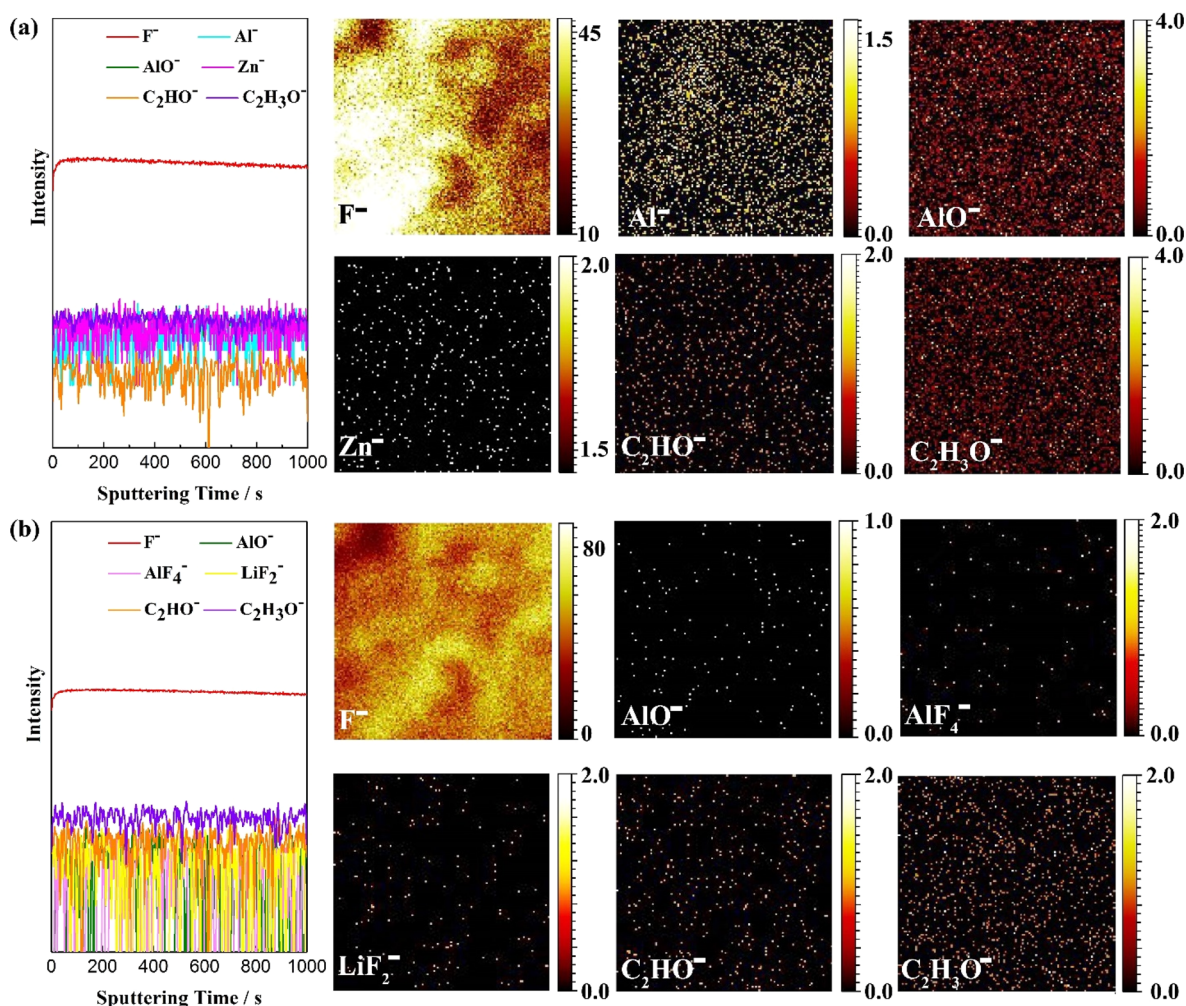
Figure 5. TOF-SIMS depth profiles and 2D mapping results of selected typical ion fragments of (a) fresh GPE-ZIF8-Al$_2$O$_3$ film (F$^-$, Al$^-$, AlO$^-$, Zn$^-$, C$_2$HO$^-$, and C$_2$H$_3$O$^-$) and (b) cycled GPE-ZIF8-Al$_2$O$_3$ film (F$^-$, AlO$^-$, AlF$_4^-$, LiF$_2^-$, C$_2$HO$^-$, and C$_2$H$_3$O$^-$) in full cells. On the surface, the TOF-SIMS sputtered area is 68 μm × 68 μm.

content depth distribution despite their low content (Figure 5a). Moreover, the corresponding 2D ion mapping results also proves the uniformity of the distribution on the surface of a fresh GPE-ZIF8-Al$_2$O$_3$ film. Similarly, the F$^-$ ion depth profile of the cycled GPE-ZIF8-Al$_2$O$_3$ film remains flat throughout the entire sputtering depth, indicating that it maintains the overall structural stability during cycling (Figure 5b). By contrast, the surface composition of the cycled GPE-ZIF8-Al$_2$O$_3$ film has changed significantly, and the generation of an AlF$_3$ component (seen from the AlF$_4^-$ fragment) can be observed, which is mainly the result of the interaction of the Al$_2$O$_3$ thin layer with the lithium salt. Also, the 2D distribution of a LiF$_2^-$ fragment observed on the surface after a cycling suggests the LiF species remains on the GPE-ZIF8-Al$_2$O$_3$ side. Affected by the complicated interface reaction during the charge/discharge process, the normalized depth profiles of AlF$_4^-$ and LiF$_2^-$ fragments present certain fluctuations. Besides the organic components of the electrolyte itself, the organic ion fragments including C$_2$HO$^-$ and C$_2$H$_3$O$^-$ in the cycled GPE-ZIF8-Al$_2$O$_3$ film are inseparable from the decomposition of organic solvents.

The applicability of the gel polymer electrolytes in the practical battery system is demonstrated by lithium metal full cells using Li-rich Mn-based layered oxides (marked as LLO)

of Li$_{1.2}$Ni$_{0.13}$Co$_{0.13}$Mn$_{0.54}$O$_2$ as cathode and lithium metal as anode to evaluate the electrochemical performance. Many studies consider that LLOs are one of the most promising cathode materials; they achieve an energy density exceeding 400 Wh kg^{-1} due to a high discharge specific capacity of more than 250 mAh g^{-1}.[58,59] However, limited by the coupling material and interface compatibility, current solid-state batteries mainly employ LiCoO$_2$, LiFePO$_4$, and Ni-rich cathode materials with narrow electrochemical windows. On the one side, to the best of our knowledge, the research of matching cathode materials within a cutoff voltage up to 4.8 V for solid-state RLBs has not yet been reported. On the other side, the liquid amount used in the batteries and mass loading of cathode materials are shown in Table S3 (Supporting Information). A relatively low liquid amount of 7.5 μL/mg$_{cathode}$ is selected for the subsequent test, which is favorable for high safety and energy density. As depicted in Figure 6a, the LLO/GPE/Li, LLO/GPE-ZIF8/Li, and LLO/GPE-ZIF8-Al$_2$O$_3$/Li batteries deliver the initial discharge specific capacities of 264.9, 277.4, and 257.5 mAh g^{-1} with the corresponding initial Coulombic efficiencies of 76.9%, 76.6%, and 77.2% at the rate of 0.2C (1C = 200 mA g^{-1}). Note that, because of the inert insulating properties of Al$_2$O$_3$, the ion conductivity in the LLO/GPE-ZIF8-Al$_2$O$_3$/Li battery will
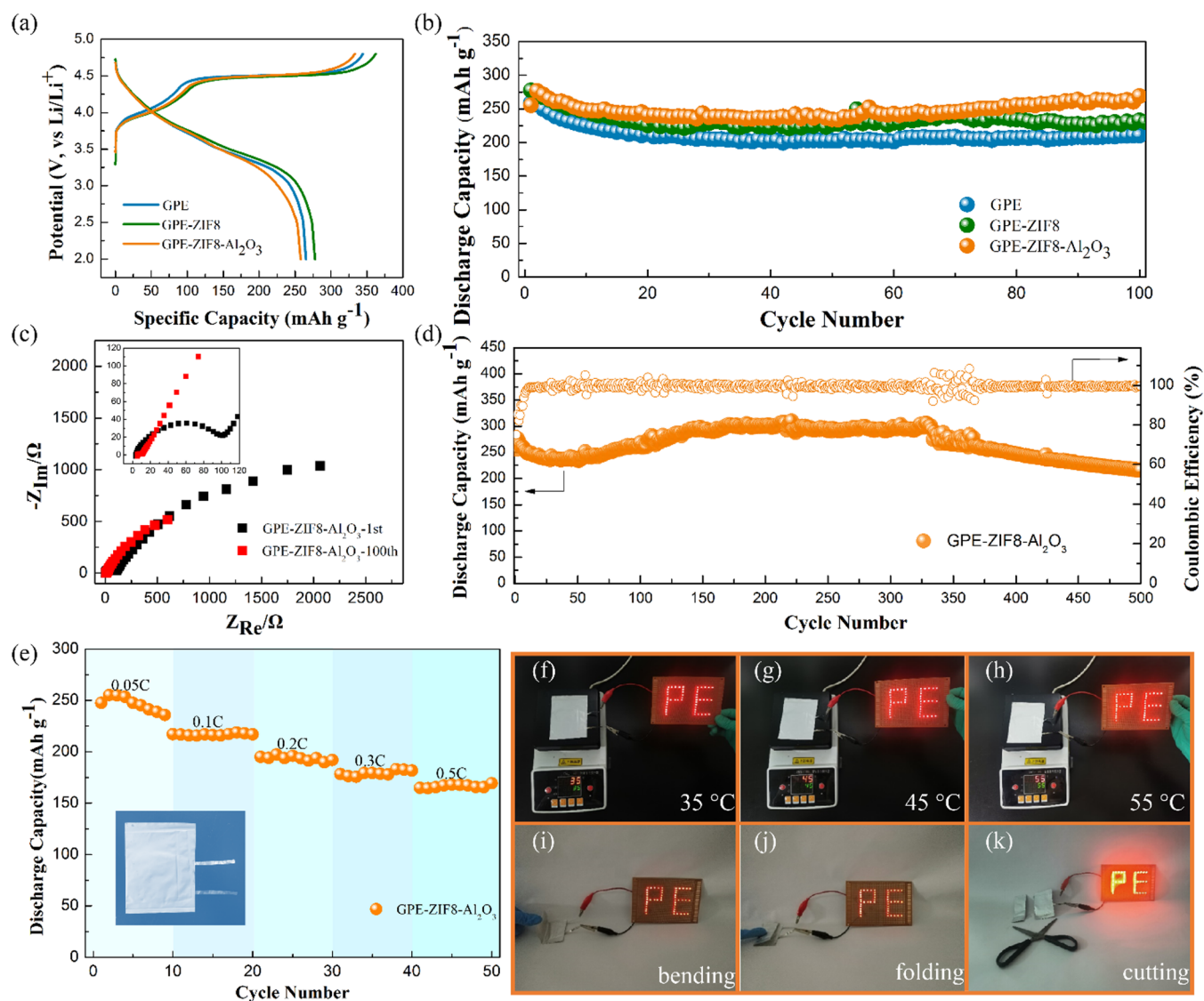
Figure 6. Electrochemical performance of full cells at room temperature. (a, b) The first charge/discharge curves and cycling stability of LLO/GPE/Li, LLO/GPE-ZIF8/Li, and LLO/GPE-ZIF8-Al$_2$O$_3$/Li batteries at the rate of 0.2C. (c) Nyquist plots of the LLO/GPE-ZIF8-Al$_2$O$_3$/Li battery at the fully charged state after the 1st and 100th cycles. (d) The long cycling performance and Coulombic efficiency of the LLO/GPE-ZIF8-Al$_2$O$_3$/Li battery. (e) Rate performance of LLO/GPE-ZIF8-Al$_2$O$_3$/Li pouch cells. Optical photographs of LLO/GPE-ZIF8-Al$_2$O$_3$/Li pouch cells under 35 °C (f), 45 °C (g), and 55 °C (h) as well as at the bending (i), folding (j), and cutting (k) states for lighting LED lamps.

inevitably be effected to a certain extent, thereby reducing its discharge capacity. After 100 cycles, the LLO/GPE-ZIF8-Al$_2$O$_3$/Li battery maintains a remarkable discharge capacity of 268.9 mAh g^{-1}, compared with 210.3 mAh g^{-1} for the LLO/GPE/Li battery and 232.9 mAh g^{-1} for the LLO/GPE-ZIF8/Li battery in Figure 6b. It is demonstrated in the Nyquist plots of the LLO/GPE-ZIF8-Al$_2$O$_3$/Li battery that the surface charge transfer resistance representing the resistance between electrolyte and electrode gets a relatively low value of only 7.0 Ω after 100 cycles, which shows a sharp decrease compared to that of the first cycle (111.6 Ω), as shown in Figure 6c. This can be attributed to the construction of a robust conductive interface during cycling, thus accelerating the charge transfer process. More importantly, even after a long-term cycle of up to 500 cycles at the 0.2C rate, the LLO/GPE-ZIF8-Al$_2$O$_3$/Li battery can still maintain an extraordinary cycle stability and excellent Coulombic efficiency. As seen from Figure 6d, it keeps an impressive discharge capacity of 216.0 mAh g^{-1} with

a capacity retention of 84.6% after 500 cycles, which is much higher than that of the LLO/GPE/Li battery (Figure S10, Supporting Information). Particularly, after a period of activation, the LLO/GPE-ZIF8-Al$_2$O$_3$/Li battery has shown a stable Coulombic efficiency close to 100% throughout the long-term cycle. Even at the 2C rate, the LLO/GPE-ZIF8-Al$_2$O$_3$/Li battery can maintain a stable and high capacity retention of 91.9% over 150 cycles (Figure S11, Supporting Information). The superior cycle life and stability in the LLO/GPE-ZIF8-Al$_2$O$_3$/Li battery results from the rapid lithium ion transport process and the interfacial stability of the lithium anode.

Furthermore, a lithium metal pouch-type cell (single layer) based on the flexibility of a GPE-ZIF8-Al$_2$O$_3$ film is assembled to investigate the rate performance and safety property, as shown in Figure 6e−k. Encouragingly, the LLO/GPE-ZIF8-Al$_2$O$_3$/Li pouch cell presents relatively outstanding cycle stability and discharge capacity rate from 0.05C to 0.5C. After

50 cycles, it can still deliver a discharge capacity of 169.5 mAh g^{-1} at 0.5C, demonstrating a fascinating application prospect. Also, the safety of lithium batteries operating under different temperatures and harsh conditions is also an important factor in evaluating their practical application performance. Apparently, as the working temperature rises from 35 and 45 to 55 °C, the pouch cell can work normally and light up the light-emitting diode (LED) lamps (Figure 6f−h). Meanwhile, the LLO/GPE-ZIF8-Al$_2$O$_3$/Li pouch cell can make the LED lamps bright even at the states of bending, folding, and cutting, suggesting its potential in flexible electronic devices (Figure 6i−k). Furthermore, the nail penetration test proves that no fire or explosion occurs in the LLO/GPE-ZIF8-Al$_2$O$_3$/Li pouch cell, and the corresponding voltage keeps a stable value (Figure S12 and Figure S13). The above results confirm the superior thermal stability and safety in the flexible LLO/GPE-ZIF8-Al$_2$O$_3$/Li pouch cell. Restricted by the ideally thin lithium anode technology, the fly in the ointment is that this work cannot assemble a pouch-type full battery that calculates the energy density in terms of the mass of the overall components in the battery. It is believed that a solid-state RLB with high energy density can be expected with the combination of the Li-rich cathode and lithium anode materials at high level in capacity.

In summary, a heterostructured gel polymer electrolyte is fabricated for long-cycle quasi-solid-state RLBs via rationally casting a ZIF-8 layer and depositing an Al$_2$O$_3$ ultrathin layer on the polymer matrix. It can not only significantly enhance the mechanical strength to achieve a homogeneous lithium deposition but also effectively improve the interfacial stability with the lithium anode. On the one side, the ZIF-8 frameworks with strong electronegativity can coordinate with Li$^+$ via an electrostatic interaction to allow the rapid transport of Li$^+$ and, meanwhile, restrict the free migration of anions through the defined intrinsic nanosized channels. On the other side, the inert Al$_2$O$_3$ would decrease the diffusion barrier and stabilize the lithium anode interface by constructing a conductive SEI film rich in fluorides. Finally, a high Li$^+$ transference number up to 0.74 is realized to inhibit the nucleation and growth of lithium dendrites, and a robust ion-conductive interface layer between electrode and electrolyte is formed to extend the cycle life. The Li symmetric cells based on a GPE-ZIF8-Al$_2$O$_3$ film display a low and stable polarization voltage with a lifespan of more than 1000 h, and the corresponding RLBs maintain a superior cycling stability with a capacity retention of 84.6% after 500 cycles at the rate of 0.2C. The heterostructured gel polymer electrolyte provides a new insight for constructing a highly stable and conductive interface toward next-generation RLBs with high performance and excellent safety.

■ ASSOCIATED CONTENT

Ⓢ Supporting Information

The Supporting Information is available free of charge at https://pubs.acs.org/doi/10.1021/acsenergylett.1c02233.

> Experimental methods, synthesis diagram, EIS spectra, and chronocurrent curves of the Li symmetric cells with different electrolytes, Li$^+$ transference numbers, ion conductivity, thickness of different electrolytes, liquid amount, EDS mapping results of GPE, XPS data for the GPE-ZIF8-Al$_2$O$_3$ film, voltage profiles of Li/GPE-ZIF8-Al$_2$O$_3$/Li symmetric cells, and electrochemical performance of the LLO/GPE/Li battery (PDF)

■ AUTHOR INFORMATION

Corresponding Author

Guoran Li − *Institute of New Energy Material Chemistry, School of Materials Science and Engineering, Renewable Energy Conversion and Storage Center, Nankai University, Tianjin 300350, China;* ⓘ orcid.org/0000-0002-6380-5725; Phone: +86-22-23500780; Email: guoranli@nankai.edu.cn

Authors

Shaolun Cui − *Institute of New Energy Material Chemistry, School of Materials Science and Engineering, Renewable Energy Conversion and Storage Center, Nankai University, Tianjin 300350, China*

Xuewen Wu − *Institute of New Energy Material Chemistry, School of Materials Science and Engineering, Renewable Energy Conversion and Storage Center, Nankai University, Tianjin 300350, China*

Yang Yang − *School of Materials Science and Engineering, Tianjin Key Lab for Rare Earth Materials and Applications, Nankai University, Tianjin 300350, China;* ⓘ orcid.org/0000-0002-9418-8563

Minfei Fei − *Department of Materials Science and Metallurgy, University of Cambridge, Cambridge CB3 0FS, United Kingdom*

Sheng Liu − *Institute of New Energy Material Chemistry, School of Materials Science and Engineering, Renewable Energy Conversion and Storage Center, Nankai University, Tianjin 300350, China;* ⓘ orcid.org/0000-0001-5933-1101

Xue-Ping Gao − *Institute of New Energy Material Chemistry, School of Materials Science and Engineering, Renewable Energy Conversion and Storage Center, Nankai University, Tianjin 300350, China;* ⓘ orcid.org/0000-0001-7305-7567

Complete contact information is available at:
https://pubs.acs.org/10.1021/acsenergylett.1c02233

Notes

The authors declare no competing financial interest.

■ REFERENCES

(1) Wu, X. W.; Cui, S. L.; Liu, S.; Li, G. R.; Gao, X. P. From Dendrites to Hemispheres: Changing Lithium Deposition by Highly Ordered Charge Transfer Channels. *ACS Appl. Mater. Interfaces* **2021**, *13*, 6249−6256.

(2) Cheng, X.; Yan, C.; Chen, X.; Guan, C.; Huang, J.; Peng, H.; Zhang, Q.; Zhang, R.; Yang, S. Implantable Solid Electrolyte Interphase in Lithium-Metal Batteries. *Chem.* **2017**, *2*, 258−270.

(3) Wang, T. S.; Liu, X.; Wang, Y.; Fan, L. Z. High Areal Capacity Dendrite-Free Li Anode Enabled by Metal-Organic Framework-Derived Nanorod Array Modified Carbon Cloth for Solid State Li Metal Batteries. *Adv. Funct. Mater.* **2021**, *31*, 2001973.

(4) Chen, X. R.; Zhao, B. C.; Yan, C.; Zhang, Q. Review on Li Deposition in Working Batteries: From Nucleation to Early Growth. *Adv. Mater.* **2021**, *33*, 2004128.

(5) Etacheri, V.; Marom, R.; Elazari, R.; Salitra, G.; Aurbach, D. Challenges in the Development of Advanced Li-Ion Batteries: A Review. *Energy Environ. Sci.* **2011**, *4*, 3243−3262.

(6) Yang, C.; Fu, K.; Zhang, Y.; Hitz, E.; Hu, L. Protected Lithium-Metal Anodes in Batteries: From Liquid to Solid. *Adv. Mater.* **2017**, *29*, 1701169.

(7) Yang, X.; Sun, Q.; Zhao, C.; Gao, X.; Adair, K. R.; Liu, Y.; Luo, J.; Lin, X.; Liang, J.; Huang, H.; Zhang, L.; Yang, R.; Lu, S. G.; Li, R. Y.; Sun, X. L. High-areal-capacity all-solid-state lithium batteries enabled by rational design of fast ion transport channels in vertically-aligned composite polymer electrodes. *Nano Energy* **2019**, *61*, 567−575.

(8) Nolan, A. M.; Liu, Y.; Mo, Y. Solid-State Chemistries Stable with High-Energy Cathodes for Lithium-Ion Batteries. *ACS Energy Lett.* **2019**, *4*, 2444−2451.

(9) Wang, G. X.; He, P. G.; Fan, L. Z. Asymmetric Polymer Electrolyte Constructed by Metal-Organic Framework for Solid-State, Dendrite-Free Lithium Metal Battery. *Adv. Funct. Mater.* **2021**, *31*, 2007198.

(10) Yang, P.; Gao, X. W.; Tian, X. L.; Shu, C. Y.; Yi, Y. K.; Liu, P.; Wang, T.; Qu, L.; Tian, B. B.; Li, M. T.; Tang, W.; Yang, B. L.; Goodenough, J. B. Upgrading Traditional Organic Electrolytes toward Future Lithium Metal Batteries: A Hierarchical Nano-SiO$_2$-Supported Gel Polymer Electrolyte. *ACS Energy Lett.* **2020**, *5*, 1681−1688.

(11) Zhou, Q.; Ma, J.; Dong, S. M.; Li, X. F.; Cui, G. L. Intermolecular Chemistry in Solid Polymer Electrolytes for High-Energy-Density Lithium Batteries. *Adv. Mater.* **2019**, *31*, 1902029.

(12) Lv, Z. L.; Zhou, Q.; Zhang, S.; Dong, S. M.; Wang, Q. L.; Huang, L.; Chen, K.; Cui, G. L. Cyano-reinforced In-Situ Polymer Electrolyte Enabling Long-Life Cycling for High-Voltage Lithium Metal Batteries. *Energy Storage Materials* **2021**, *37*, 215−223.

(13) Xu, G. J.; Zhao, M.; Xie, B.; Wang, X.; Jiang, M. M.; Guan, P.; Han, P. X.; Cui, G. L. A Rigid-Flexible Coupling Gel Polymer Electrolyte towards High Safety Flexible Li-Ion Battery. *J. Power Sources* **2021**, *499*, 229944.

(14) Ye, L. H.; Li, X. A Dynamic Stability Design Strategy for Lithium Metal Solid State Batteries. *Nature* **2021**, *593*, 218−222.

(15) Chi, X.; Li, M.; Di, J.; Bai, P.; Song, L.; Wang, X.; Li, F.; Liang, S.; Xu, J.; Yu, J. A Highly Stable and Flexible Zeolite Electrolyte Solid-State Li-Air Battery. *Nature* **2021**, *592*, 551−557.

(16) Le, H. T.; Ngo, D. T.; Kalubarme, R. S.; Cao, G.; Park, C. N.; Park, C. J. Composite Gel Polymer Electrolyte Based on Poly-(vinylidene fluoride-hexafluoropropylene) (PVDF-HFP) with Modified Aluminum Doped Lithium Lanthanum Titanate (A-LLTO) for High-Performance Lithium Rechargeable Batteries. *ACS Appl. Mater. Interfaces* **2016**, *8*, 20710−20719.

(17) Hao, Z. D.; Wu, Y.; Zhao, Q.; Tang, J. D.; Zhang, Q. Q.; Ke, X. X.; Liu, J. B.; Jin, Y. H.; Wang, H. Functional Separators Regulating Ion Transport Enabled by Metal-Organic Frameworks for Dendrite-Free Lithium Metal Anodes. *Adv. Funct. Mater.* **2021**, *31*, 2102938.

(18) Liu, Y.; Hu, R.; Zhang, D.; Liu, J.; Liu, F.; Cui, J.; Lin, Z.; Wu, J.; Zhu, M. Constructing Li-Rich Artificial SEI Layer in Alloy-Polymer Composite Electrolyte to Achieve High Ionic Conductivity for All Solid-State Lithium Metal Batteries. *Adv. Mater.* **2021**, *33*, 2004711.

(19) Wang, L. L.; Sun, X. W.; Ma, J.; Chen, B. B.; Li, C.; Li, J. D.; Chang, L.; Yu, X. R.; Chan, T. S.; Hu, Z. W.; Noked, M.; Cui, G. L. Bidirectionally Compatible Buffering Layer Enables Highly Stable and Conductive Interface for 4.5 V Sulfide-Based All-Solid-State Lithium Batteries. *Adv. Energy Mater.* **2021**, *11*, 2100881.

(20) Yu, X. R.; Wang, L. L.; Ma, J.; Sun, X. W.; Zhou, X. H.; Cui, G. L. Selectively Wetted Rigid−Flexible Coupling Polymer Electrolyte Enabling Superior Stability and Compatibility of High-Voltage Lithium Metal Batteries. *Adv. Energy Mater.* **2020**, *10*, 1903939.

(21) Lv, Z. L.; Tang, Y.; Dong, S. M.; Zhou, Q.; Cui, G. L. Polyurethane-Based Polymer Electrolytes for Lithium Batteries: Advances and Perspectives. *Chem. Eng. J.* **2022**, *430*, 132659.

(22) Fan, L.; Wei, S. Y.; Li, S. Y.; Li, Q.; Lu, Y. Y. Recent Progress of the Solid-State Electrolytes for High-Energy Metal-Based Batteries. *Adv. Energy Mater.* **2018**, *8*, 1702657.

(23) Lin, D. C.; Liu, W.; Liu, Y. Y.; Lee, H. R.; Hsu, P. C.; Liu, K.; Cui, Y. High Ionic Conductivity of Composite Solid Polymer Electrolyte via In Situ Synthesis of Monodispersed SiO2 Nanospheres in Poly(ethylene oxide). *Nano Lett.* **2016**, *16*, 459−465.

(24) Xiao, C. F.; Kim, J. H.; Cho, S. H.; Park, Y. C.; Kim, M. J.; Chung, K. B.; Yoon, S. G.; Jung, J. W.; Kim, I. D.; Kim, H. S. Ensemble Design of Electrode−Electrolyte Interfaces: Toward High-Performance Thin-Film All-Solid-State Li−Metal Batteries. *ACS Nano* **2021**, *15*, 4561−4575.

(25) Jiang, T.; He, P.; Wang, G.; Shen, Y.; Nan, C. W.; Fan, L. Z. Solvent-Free Synthesis of Thin, Flexible, Nonflammable Garnet-Based Composite Solid Electrolyte for All-Solid-State Lithium Batteries. *Adv. Energy Mater.* **2020**, *10*, 1903376.

(26) Li, Z.; Huang, H. M.; Zhu, J. K.; Wu, J. F.; Yang, H.; Wei, L.; Guo, X. Ionic Conduction in Composite Polymer Electrolytes: Case of PEO:Ga-LLZO Composites. *ACS Appl. Mater. Interfaces* **2019**, *11*, 784−791.

(27) Liu, W.; Lee, S. W.; Lin, D. C.; Shi, F. F.; Wang, S.; Sendek, A. D.; Cui, Y. Enhancing Ionic Conductivity in Composite Polymer Electrolytes with Well-Aligned Ceramic Nanowires. *Nat. Energy* **2017**, *2*, 17035.

(28) Liu, X. Q.; Peng, S.; Gao, S. Y.; Cao, Y. C.; You, Q. L.; Zhou, L. Y.; Jin, Y. C.; Liu, Z. H.; Liu, J. Electric-Field-Directed Parallel Alignment Architecting 3D Lithium-Ion Pathways within Solid Composite Electrolyte. *ACS Appl. Mater. Interfaces* **2018**, *10*, 15691−15696.

(29) Qian, J.; Li, Y.; Zhang, M.; Luo, R.; Wang, F.; Ye, Y.; Xing, Y.; Li, W.; Qu, W.; Wang, L.; Li, L.; Li, Y.; Wu, F.; Chen, R. Protecting Lithium/Sodium Metal Anode with Metal-Organic Framework Based Compact and Robust Shield. *Nano Energy* **2019**, *60*, 866−874.

(30) Huo, H.; Wu, B.; Zhang, T.; Zheng, X.; Ge, L.; Xu, T.; Guo, X.; Sun, X. Anion-Immobilized Polymer Electrolyte Achieved by Cationic Metal-Organic Framework Filler for Dendrite-Free Solid-State Batteries. *Energy Storage Mater.* **2019**, *18*, 59−67.

(31) Sun, Y. Y.; Liu, S.; Hou, Y. K.; Li, G. R.; Gao, X. P. In-Situ Surface Modification to Stabilize Ni-Rich Layered Oxide Cathode with Functional Electrolyte. *J. Power Sources* **2019**, *410*, 115−123.

(32) Blake, A. J.; Kohlmeyer, R. R.; Hardin, J. O.; Carmona, E. A.; Maruyama, B.; Berrigan, J. D.; Huang, H.; Durstock, M. F. 3D Printable Ceramic-Polymer Electrolytes for Flexible High-Performance Li-Ion Batteries with Enhanced Thermal Stability. *Adv. Energy Mater.* **2017**, *7*, 1602920.

(33) Xu, Z.; He, D.; Xie, X. Poly(ethylene oxide)-based electrolytes for lithium-ion batteries. *J. Mater. Chem. A* **2015**, *3*, 19218−19253.

(34) Sun, Y. Y.; Wang, Y. Y.; Li, G. R.; Liu, S.; Gao, X. P. Metalophilic Gel Polymer Electrolyte for in Situ Tailoring Cathode/Electrolyte Interface of High-Nickel Oxide Cathodes in Quasi-Solid-State Li-Ion Batteries. *ACS Appl. Mater. Interfaces* **2019**, *11*, 14830−14839.

(35) Tang, J.; Salunkhe, R. R.; Liu, J.; Torad, N. L.; Imura, M.; Furukawa, S.; Yamauchi, Y. Thermal Conversion of Core-Shell Metal-Organic Frameworks: A New Method for Selectively Functionalized Nanoporous Hybrid Carbon. *J. Am. Chem. Soc.* **2015**, *137*, 1572−1580.

(36) Lu, G.; Li, S.; Guo, Z.; Farha, O. K.; Hauser, B. G.; Qi, X.; Wang, Y.; Wang, X.; Han, S.; Liu, X.; DuChene, J. S.; Zhang, H.; Zhang, Q.; Chen, X.; Ma, J.; Loo, S. C. J.; Wei, W. D.; Yang, Y.; Hupp, J. T.; Huo, F. Imparting Functionality to A Metal-Organic Framework Material by Controlled Nanoparticle Encapsulation. *Nat. Chem.* **2012**, *4*, 310−316.

(37) Lin, C. R.; Zhang, H.; Song, Y. Z.; Zhang, Y.; Yuan, J. J.; Zhu, B. K. Carboxylated Polyimide Separator with Excellent Lithium Ion Transport Properties for A High-Power Density Lithium-Ion Battery. *J. Mater. Chem. A* **2018**, *6*, 991−998.

(38) Chen, L.; Li, W. X.; Fan, L. Z.; Nan, C. W.; Zhang, Q. Intercalated Electrolyte with High Transference Number for Dendrite-Free Solid-State Lithium Batteries. *Adv. Funct. Mater.* **2019**, *29*, 1901047.

(39) Wang, L.; Wang, Y.; Zhang, F.; Bai, Y.; Ding, L. Syntheses and Properties of the PET-co-PEA Copolyester. *J. Appl. Polym. Sci.* **2017**, *134*, 44967.

(40) Liang, W.; Hou, J.; Fang, X.; Bai, F.; Zhu, T.; Gao, F.; Wei, C.; Mo, X.; Lang, M. Synthesis of Cellulose Diacetate Based Copolymer Electrospun Nanofibers for Tissues Scaffold. *Appl. Surf. Sci.* **2018**, *443*, 374−381.

(41) Jian, M.; Liu, B.; Zhang, G.; Liu, R.; Zhang, X. Adsorptive Removal of Arsenic from Aqueous Solution by Zeolitic Imidazolate Framework-8 (ZIF-8) Nanoparticles. *Colloids Surf., A* **2015**, *465*, 67− 76.

(42) Hu, Y.; Kazemian, H.; Rohani, S.; Huang, Y.; Song, Y. In Situ High Pressure Study of ZIF-8 by FTIR Spectroscopy. *Chem. Commun.* **2011**, *47*, 12694−12696.

(43) Hayashi, M.; Lee, D. T.; Mello, M. D.; Boscoboinik, J. A.; Tsapatsis, M. ZIF-8 Membrane Permselectivity Modification by Manganese(II) Acetylacetonate Vapor Treatment. *Angew. Chem., Int. Ed.* **2021**, *60*, 9316−9320.

(44) Ng, S.; Iffelsberger, C.; Michalička, J.; Pumera, M. Atomic Layer Deposition of Electrocatalytic Insulator Al_2O_3 on Three-Dimensional Printed Nanocarbons. *ACS Nano* **2021**, *15*, 686−697.

(45) Hiller, M. M.; Joost, M.; Gores, H. J.; Passerini, S.; Wiemhöfer, H. D. The Influence of Interface Polarization on the Determination of Lithium Transference Numbers of Salt in Polyethylene Oxide Electrolytes. *Electrochim. Acta* **2013**, *114*, 21−29.

(46) Zhu, Z. W.; Wang, Z. Y.; Liu, S.; Li, G. R.; Gao, X. P. Uniform Lithium Plating within 3D Cu Foam Enabled by Ag Nanoparticles. *Electrochim. Acta* **2021**, *379*, 138152.

(47) Yang, C. P.; Yin, Y. X.; Zhang, S. F.; Li, N. W.; Guo, Y. G. Accommodating Lithium into 3D Current Collectors with a Submicron Skeleton towards Long-Life Lithium Metal Anodes. *Nat. Commun.* **2015**, *6*, 8058.

(48) Li, Q.; Cao, Z.; Wahyudi, W.; Liu, G.; Park, G. T.; Cavallo, L.; Anthopoulos, T. D.; Wang, L.; Sun, Y. K.; Alshareef, H. N.; Ming, J. Unraveling the New Role of an Ethylene Carbonate Solvation Shell in Rechargeable Metal Ion Batteries. *ACS Energy Lett.* **2021**, *6*, 69−78.

(49) Kushima, A.; So, K. P.; Su, C.; Bai, P.; Kuriyama, N.; Maebashi, T.; Fujiwara, Y.; Bazant, M. Z.; Li, J. Liquid Cell Transmission Electron Microscopy Observation of Lithium Metal Growth and Dissolution: Root Growth, Dead Lithium and Lithium Flotsams. *Nano Energy* **2017**, *32*, 271−279.

(50) Yang, Y.; Liu, C. Y.; Lv, Z. H.; Yang, H.; Zhang, Y. F.; Ye, M. H.; Chen, L. B.; Zhao, J. B.; Li, C. C. Synergistic Manipulation of Zn^{2+} Ion Flux and Desolvation Effect Enabled by Anodic Growth of a 3D ZnF_2Matrix for Long-Lifespan and Dendrite-Free Zn Metal Anodes. *Adv. Mater.* **2021**, *33*, 2007388.

(51) Xiao, Z. X.; Cui, S. L.; Wang, Y. Y.; Liu, S.; Li, G. R.; Gao, X. P. Enabling $LiNi_{0.88}Co_{0.09}Al_{0.03}O_2$ Cathode Materials with Stable Interface by Modifying Electrolyte with Trimethyl Borate. *ACS Sustainable Chem. Eng.* **2021**, *9*, 1958−1968.

(52) Liu, J.; Yang, Y.; Yu, P.; Li, Y.; Shao, H. Electrochemical Characterization of $LaNi_{5-x}Al_x$ (x = 0.1−0.5) in the Absence of Additives. *J. Power Sources* **2006**, *161*, 1435−1442.

(53) Jiao, S.; Ren, X.; Cao, R.; Engelhard, M. H.; Liu, Y.; Hu, D.; Mei, D.; Zheng, J.; Zhao, W.; Li, Q.; Liu, N.; Adams, B. D.; Ma, C.; Liu, J.; Zhang, J. G.; Xu, W. Stable Cycling of High-Voltage Lithium Metal Batteries in Ether Electrolytes. *Nat. Energy* **2018**, *3*, 739−746.

(54) Lu, Y. Y.; Tu, Z. Y.; Archer, L. A. Stable Lithium Electrodeposition in Liquid and Nanoporous Solid Electrolytes. *Nat. Mater.* **2014**, *13*, 961−969.

(55) Tu, Z. Y.; Zachman, M. J.; Choudhury, S.; Wei, S. Y.; Ma, L.; Yang, Y.; Kourkoutis, L. F.; Archer, L. A. Nanoporous Hybrid Electrolytes for High-Energy Batteries Based on Reactive Metal Anodes. *Adv. Energy Mater.* **2017**, *7*, 1602367.

(56) Jung, S. C.; Han, Y. K. How Do Li Atoms Pass through the Al2O3 Coating Layer during Lithiation in Li-ion Batteries? *J. Phys. Chem. Lett.* **2013**, *4*, 2681−2685.

(57) Zhou, K.; Xie, Q.; Li, B.; Manthiram, A. An In-Depth Understanding of the Effect of Aluminum Doping in High-Nickel Cathodes for Lithium-Ion Batteries. *Energy Storage Materials* **2021**, *34*, 229−240.

(58) Cui, S. L.; Gao, M. Y.; Li, G. R.; Gao, X. P. Insights into Li-Rich Mn-Based Cathode Materials with High Capacity: from Dimension to Lattice to Atom. *Adv. Energy Mater.* **2021**, *11*, 2003885.

(59) Cui, S. L.; Zhang, X.; Wu, X. W.; Liu, S.; Zhou, Z.; Li, G. R.; Gao, X. P. Understanding the Structure-Performance Relationship of Lithium-Rich Cathode Materials from an Oxygen-Vacancy Perspective. *ACS Appl. Mater. Interfaces* **2020**, *12*, 47655−47666.